Bulletin of the Mineral Research and Exploration

http://bulletin.mta.gov.tr

Comparative analysis of water and carbon dioxide injection for the thermohydraulics of an EGS project in Dikili Geothermal Field, Türkiye

Ali Cemal BENİM[a] and Aydın ÇİÇEK[b*]

[a]*Düsseldorf University of Applied Sciences, Department of Mechanical and Process Technology, Center of Flow Simulation, Düsseldorf, Germany.*
[b]*General Directorate of Mineral Research and Exploration of Türkiye, Department of Energy Raw Materials, Ankara, Türkiye.*

Research Article

Keywords:
EGS, Thermohydraulics, Computational Analysis, Supercritical Carbon Dioxide.

ABSTRACT

A comparative numerical analysis of the thermohydraulics of an enhanced geothermal system (EGS) project in Türkiye in Dikili area is presented. The fractured granodiorite is modelled as porous media, utilizing the numerically suggested data of other authors for the corresponding hydraulic characteristics. As the heat transmission fluid, two different mediums are alternatively considered. These are the more classical medium, water and the supercritical carbon dioxide (sCO_2). Transient calculations are performed for a time period of twenty years, comparing the temporally developing results obtained for water and sCO_2 with each other. Based on modeling parameters and assumptions, higher production temperatures are observed with sCO_2, in comparison to water, implying an advantage for sCO_2 usage as a working fluid in EGS. This is accompanied by the further advantage of a lower pressure drop for sCO_2. On the other hand, the temperature advantage is relativized by the lower specific heat capacity of sCO_2 causing a decrease in the production thermal power. In general, the present results are found to be encouraging for a further and more detailed analysis of the employment of sCO_2 as working fluid in EGS.

Received Date: 22.08.2022
Accepted Date: 27.04.2023

1. Introduction

Türkiye attracted many scientists due to its spectacular geology during the last century. Neotectonics, active tectonics and related geothermal potential of western Anatolia has scientifically been a hot place since the 2007 following the enactment of the "Geothermal Resources and Natural Mineral Waters (Law No: 5686)". Dikili geothermal field, located nearly 75 km north of İzmir city in westernmost Türkiye, is a significant conventional geothermal field (Figure 1). The Dikili geothermal field is bounded by Madra mountain to the north, Karadağ mountain to the south and Yuntdağ mountain to the southwest (Figure 2).

Although there are a number of formations in the study area, geological units of the geothermal field are subdivided here into 4 units for the sake of simplicity (Figure 2). From older to younger, (1) Pre-Tertiary (Permian-Triassic) basement rocks with siltstone, mudstone, silty limestone and limestones, (2) late Oligocene to early.

Miocene Kozak magmatic complex composed mainly of granodiorites, (3) early Miocene to Quaternary basic to asidic volcanics and sedimentary rocks (siltstone, mudstone and limestones) and (4) Quaternary-aged relatively loose sediments.

Citation Info: Benim, A. C., Çiçek, A. 2023. Comparative analysis of water and carbon dioxide injection for the thermohydraulics of an EGS project in Dikili Geothermal Field, Türkiye. Bulletin of the Mineral Research and Exploration 171, 91-105. https://doi.org/10.19111/bulletinofmre.1288731

**Corresponding author: Aydın ÇİÇEK, aydincicek2003@gmail.com*

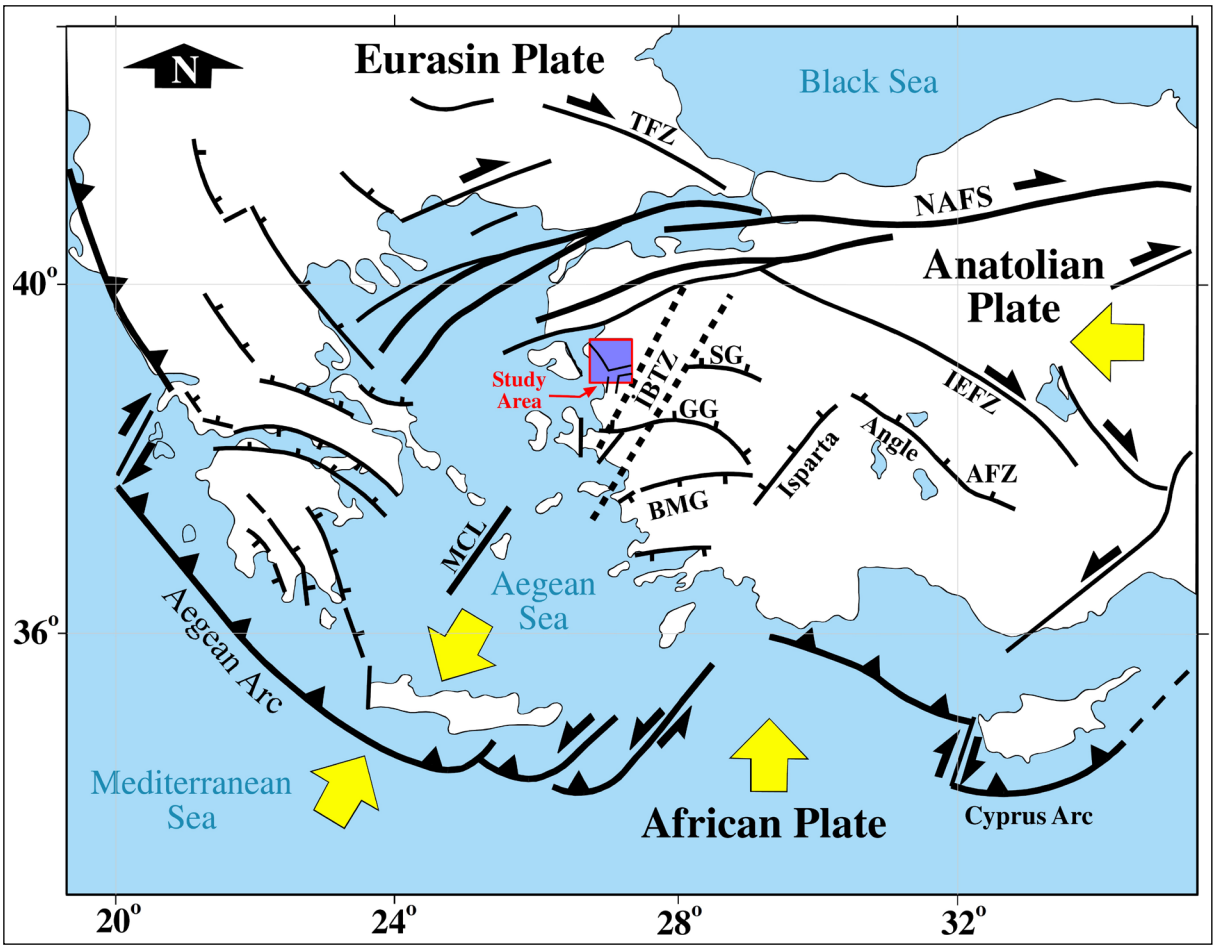

Figure 1- Simplified map showing the major (plate) tectonic elements and configuration of the Aegean region. NAFS, North Anatolian Fault System; TGF, Tuz Gölü Fault; IEFZ, İnönü-Eskişehir Fault Zone; AFZ, Akşehir Fault Zone; BMG, Büyük Menderes Graben; GG, Gediz Graben; SG, Simav Graben; MCL, Mid-Cycladic Lineament; TFZ, Thrace Fault Zone; İBTZ, İzmir-Balıkesir Transfer Zone (Re-drawn from Uzel, 2013).

The geothermal potential and the tectonics of the study area is also previously studied well by many researchers (e.g. JICA, 1987; Hou et al., 2015; Baba et al., 2022; Gürer, 2023). The Dikili geothermal field tectonically lies in the junction of Altınova, Bakırçay and Çandarlı basins (Figure 2). In addition, the area seems to be affected partly by strike-slip İzmir-Balıkesir Transfer Zone (İBTZ) (Figure 1) (Altunkaynak and Yılmaz, 1998; Uzel, 2013; Hou et al., 2015). Based on the lineament analysis done here using 1/25,000 and 1/250,000 topographic maps, it seems that the study area is mainly dominated by the NE-SW and relatively less dominated by the NW-SE-trending structural features (Figure 3).

The reservoir rocks of conventional geothermal system in the Dikili geothermal field is made of mainly by volcanics (Parlaktuna and Avşar, 2014). Although JICA (1987) proposed that the recharge area is located in the north (Madra mountains), the Yuntdağ and Karadağ mountains have also some potential as recharge area based on the surface geology and topography. The geothermal waters found inside the Dikili geothermal field are meteoric in origin based on some isotopic studies (JICA, 1987).

Baba et al. (2022) reported 27 geothermal wells with various depths and 4 springs as of February 2022. According to them, surface temperatures and flow rates of the springs vary between 57-80 ºC and 2-180 l/s, of geothermal wells between 37-131.5 ºC and 15-60 l/s, respectively. Although there are many economically producing conventional geothermal wells, some hot and economically dry wells were reported as well

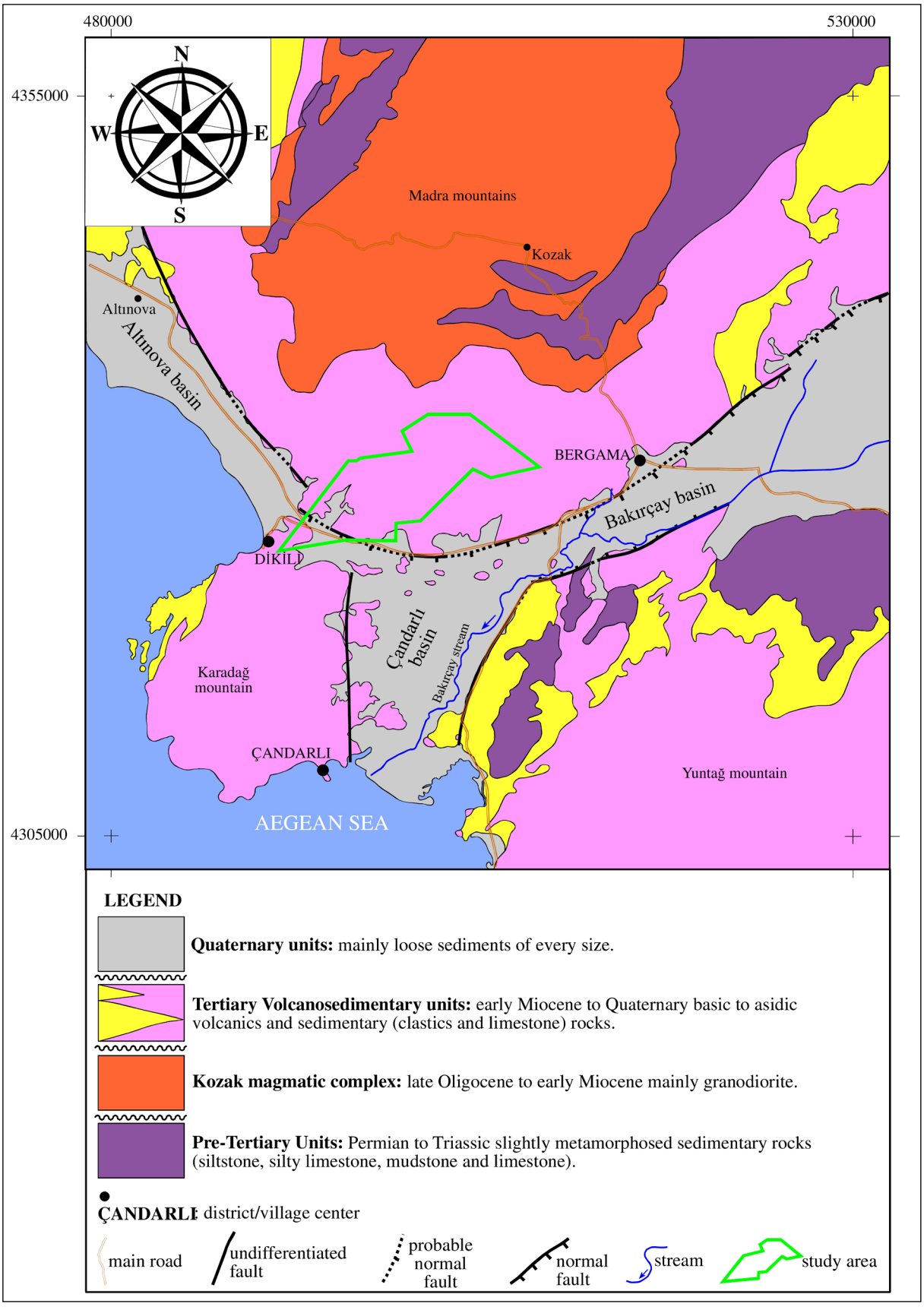

Figure 2- Simplified geological map of the study area and its vicinity (simplified from JICA, 1987).

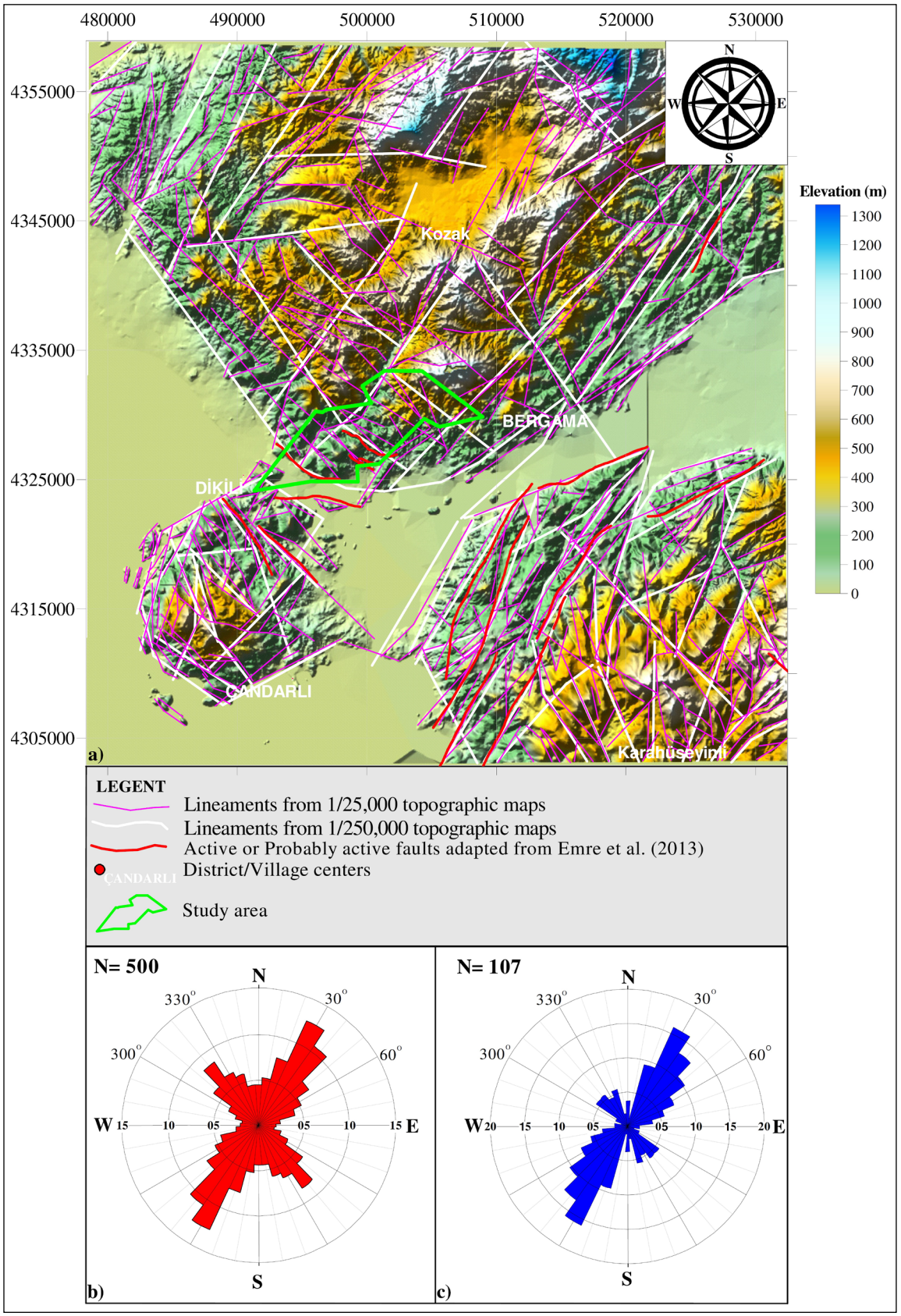

Figure 3- DEM of the study area and its vicinity, b) rose diagram of the lineament anaylsis obtained from 1/25.000 topographic maps and c) 1/250.000 topographic maps.

(Baba et al., 2022; Parlaktuna and Avşar, 2014). The bottom hole temperatures of the wells reach up to 135 ºC at a depth of 1,500 m (Yılmazer et al., 1990).

Based on previous studies, some radioactive element-bearing rocks such as Yuntdağ volcanics and Kozak granodiorite are common in the study area (Yarar et al, 2005). In addition, deep-circulation related convection cells as evidenced by fluctuating geothermal gradients at shallow depths are widespread (Parlaktuna and Avşar, 2014). Based on this, the heat sources may at least be attributed to radioactivity and deep-circulated meteoric waters (i.e. convective geothermal system).

Hou et al. (2015) presented the preliminary geology, geophysics and geochemistry results of the study area. They used FLAC3D software, a code adapted for geotechnical analysis, in their study (FLAC3D, 2019). In modelling fracturing, the strain-hardening/-softening ubiquitous-joint model was used, in which the mechanical behavior of matrix and joint was described by the Mohr-Coulomb criteria with a tension cutoff that can harden or soften according to specific laws. Hou et al. (2015) did not provide any detailed mathematical and numerical modelling aspects of the study for the modeling the flow. More detailed investigations of the thermohydraulics of the EGS project, with emphasis on numerical modelling aspects, such as grid independence and domain size, spatial and temporal resolution, were provided by Benim et al. (2018 *a, b*). Turan et al. (2021) calculated the EGS potential of the study area using probabilistic assessment method. In this study, we focus on the classical type Enhanced Geothermal Systems (EGS) potential of a part of the Dikili geothermal field by comparing water and sCO_2 as a working fluid using numerical code Ansys Fluent 18.0 (Figure 4). Here we present the results, advantages and disadvantages of sCO_2 as a working fluid over water in a classical type EGS of Çiçek (2020) for the first time in Türkiye.

The above-mentioned studies on the EGS project were carried out for water as the working fluid. If super critical carbon dioxide sCO_2 is used as heat transfer fluid, the utilization of geothermal energy can advantageously be combined with simultaneous sequestration of the carbon dioxide, a greenhouse gas (Brown, 2000). Therefore, the use of carbon dioxide in EGS is among the current hot research topics in energy technology and is being studied by a number of researchers. A higher capacity to use CO_2 as a working fluid compared to water was predicted by Pruess (2006, 2010) for an analyzed case. A study is presented on the problem of clogging due to high salinity working fluid by Borgia et al. (2012). A more recent study presented by Liu et al. (2019) comparing the efficiencies of water and sCO_2 as working fluid in a Chinese case. An investigation into the utilization of sCO_2 in the above-mentioned EGS project in Dikili area, in İzmir, Türkiye, was recently presented by Benim and Çiçek (2022). The present investigation is a continuation of this work, where a more detailed analysis is presented. The main difference to the previous study lies in the postprocessing and interpretion of the results. In the present paper, the temperature fields of sCO_2 injection are compared directly with those of water injection, and in additional planes that reveal the penetration of the temperature wave in the direction perpendicular to the plane of the walls, which were not the case in Benim and Çiçek (2022). In addition, a comparative analysis between sCO_2 and water injection is presented for the useful thermal power, total produced energy as function of time, as well as the required pumping power, which were not elaborated in Benim and Çiçek (2022).

In the studies of other authors on CO_2 injection in EGS projects mentioned above, specialized software designed for geothermal reservoir calculations, such as TOUGH2 (Pruess, 1991) and T2Well (Pan and Oldenburg, 2014) were used. As it was the case in the previous work of the Benim et al. (2018*a, b*), Benim and Çiçek (2022), the current analysis is based on the general-purpose Computational Fluid Dynamics (CFD) Software ANSYS Fluent 18.0 (ANSYS Fluent, 2018).

2. The Investigated EGS Configuration and Solution Domain Definition

The envisaged injection-production configuration is a triplet one, where two production wells are symmetrically arranged around a single injection well, as depicted in Figure 4a. The configuration exhibits two symmetry planes, which are also indicated in the figure. These are utilized in the mathematical modelling to reduce the computational overhead. Thus,

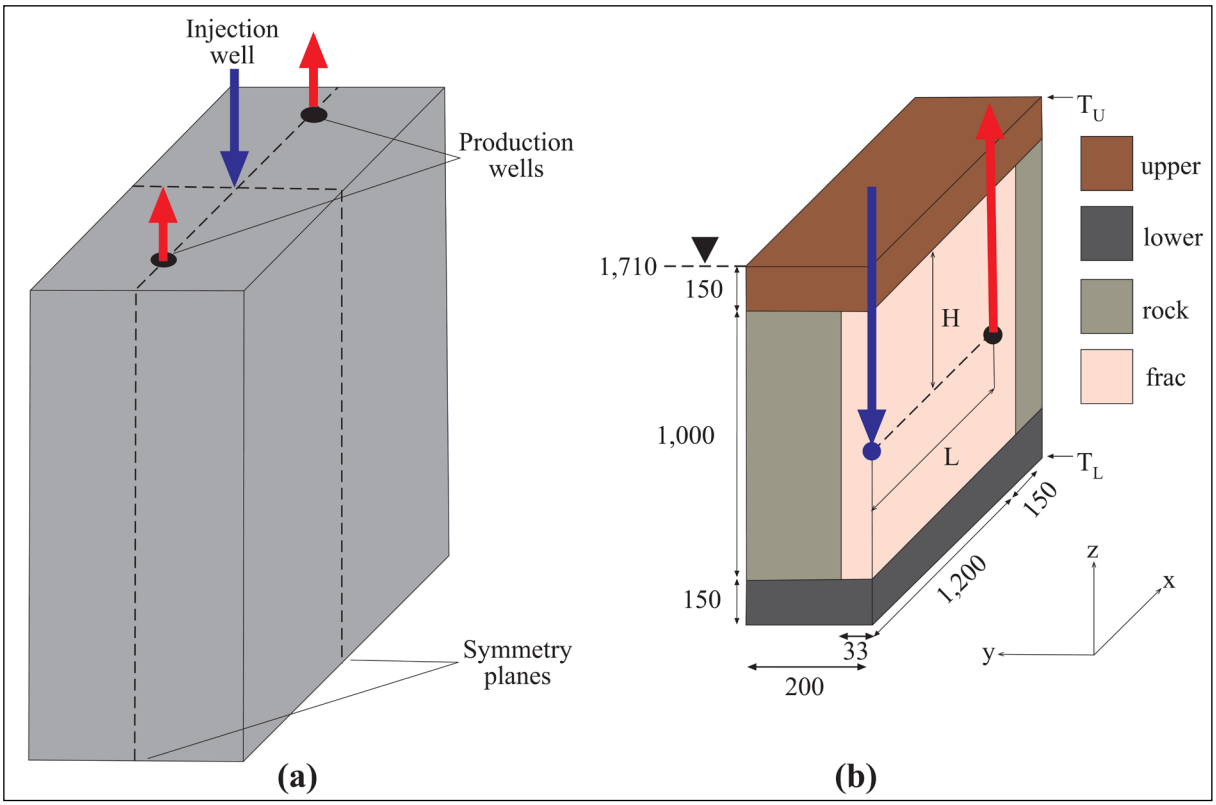

Figure 4- The considered EGS configuration; a) locations of production and injection wells, b) solution domain (in meter) and rock zones.

a quarter of the region shown in Figure 4a is defined to be the solution domain, which is bounded by two symmetry planes. The solution domain is illustrated in Figure 4b, where the dimensions (in meter) as well as the topology of the assumed rock structures are also indicated, along with the orientation of the used Cartesian coordinate system.

The dimensions of the fractured region (1200 x 33 x 1000 m) are borrowed from Hou et al. (2015). Except the symmetry planes, there is, of course, a certain arbitrariness in choosing the positions of the surfaces that bound the solution domain. They should be chosen sufficiently far away from the region of interest, so that the applied boundary conditions don't interfere with the process, i.e. don't falsify the results. In a previous study, a study was carried out by Benim et al. (2018*a*) by considering different domain sizes in the same configuration and it was ensured that the present choice (Figure 4b) provides an adequate domain size. Please also note that the upper horizontal boundary of the domain (Figure 4b) is not positioned at the ground surface but a position at 1710 m depth.

3. Mathematical and Numerical Modelling Outline

The Computational Fluid Dynamics (CFD) software Fluent (ANSYS Fluent, 2018) is used during computational modelling. The software uses the Finite Volume Method (FVM) of discretization (Versteeg and Malalasekera, 2007).

3.1. Mathematical Modelling

The solution domain contains solid and fluid materials. Although the real physics may imply a certain "dynamical" fluid-solid interaction, the solids are assumed to be non-deformable. Possible chemical interactions between the fluid and solids are also neglected. Thus, the fluid-solid interaction is solely "thermal" in nature in the present model. The total transport processes that are involved in the solution domain are of energy, mass and momentum described by the corresponding differential balance equations (Bird et al., 2006). Mass, momentum as well as conductive and convective energy transport processes govern the flow of the heat transfer fluid. The energy transport from the hot solid into the colder fluid occurs

by means of conduction and convection heat transfer (Bhattacharyya et al., 2016) through the surfaces of the fractures in the rocks. This energy extraction by the fluid and the corresponding local temperature drop triggers energy transport i.e. heat transfer, from the farther and hotter rock regions towards the colder zones, feeding the system. In the present case, due to the extremely large disparity between the geometric scales of the fractures and the solution domain, it is not possible to model the heat transmission by resolving fluid-solid interfaces, as it is commonly done in many other smaller scale convective heat transfer applications (Bhattacharyya et al., 2016). Therefore, the rocks are modelled as porous medium, where the individual fractures are not geometrically resolved, but their integral effect in larger scales is accounted for by means of characterizing parameters such as the porosity and permeability, through which the corresponding transport equations are accordingly amended (Civan, 2011).

Turbulent flow in porous media flow is a further challenging topic (Wood et al., 2020), and commonly employed turbulence modelling approaches (Benim, 1990; Xia et al., 1997) cannot readily be adopted to flow in porous media. In the current modelling, the influence of flow turbulence is neglected. This assumption can be seen to be justified, at least in part, by the very low superficial and physical velocities expected within the tiny fractures. According to the Darcy law, the porous solid region influence onto the fluid hydrodynamics is accounted for by introducing a momentum sink into the Navier-Stokes equations that corresponds to a static pressure drop (Whitaker, 1986).

3.2. Material Properties

For the characterizing parameters of the porous medium, the data provided in Hou et al. (2015) is utilized. In reference to the rock regions depicted in Figure 4b, the employed values are listed in Table 1, where the given values are assumed to remain constant within each zone. The permeabilities and porosities are generally rather low as shown in Table 1. It should also be noted that the permeability of the fractured zone (frac) is anisotropic unlike the remaining zones. In the fractured zone, the permeability is several orders of magnitude larger in the main fracturing direction compared to the other directions.

Table 1- Porosities and permeabilities (in m^2) of rock zones (Figure 1b).

	Upper	**Frac**	**Rock**	**Lower**
porosity	0.013	0.02	0.02	0.02
permeability (x)	4×10^{-18}	1×10^{-13}	4×10^{-18}	4×10^{-18}
permeability (y)	4×10^{-18}	4×10^{-18}	4×10^{-18}	4×10^{-18}
permeability (z)	4×10^{-18}	4×10^{-14}	4×10^{-18}	4×10^{-18}

An important component of the mathematical modelling is the material properties of the considered media. For the case with water as the heat transfer medium, compressibility of the water is neglected. The water used as the working fluid may evaporate inside the system due to high temperatures and can also be followed by a condensation as it is known to occur in some EGS projects. Nevertheless, in the current configuration, an analysis of the prevailing pressures and temperatures with respect to the thermodynamic water properties has implied that the water remains in liquid phase throughout modeling. The compressibility of injected supercritical Carbon Dioxide (sCO_2) is also considered during modeling as described below. The used material properties, namely the specific heat capacity (c), thermal conductivity (λ), density (ρ) and dynamic viscosity (μ) of water are assumed to be constant. The thermophysical rock properties are also considered to be constant. The used material properties for the water and solid rocks are summarized in Table 2.

Table 2- Material properties of water and solid rocks.

	μ [Pa·s]	ρ [kg/m^3]	c [J/(kg·K)]	λ [W/(m.K)]
water	0.00019	940	4176	0.717
rock	-	2670	965	2.83

Special attention is required to model the thermophysical material properties of sCO_2. In the current modeling, NIST (National Institute of Standards and Technology) Thermodynamic and Transport Properties Refrigrants and Refrigrant Mixtures Database Version 9.1 (REFROP v9.1) (Lemmon et al., 2018) is used for the thermophysical behavior of the sCO_2. Thus, in calculating the case with sCO_2 as the heat transfer fluid, the pressure and temperature dependence of the material properties are accurately considered. Here, a further important question is, if the medium remains within the

supercritical regime throughout complete solution domain, or if local temperature and pressure values cause a local transition into a different state such as superheated gas or subcooled liquid. The occurrence of such transitions would cause some problems in numerical analysis. The values for the critical pressure and temperature carbon dioxide (CO_2) are known to be 73.82 bar and 31.04°C, respectively. The superheated state prevails above this. Since the lowest temperature in the system is 60°C (inlet temperature of the heat transfer liquid), a deviation from the superheated state can only happen if the pressure attains to a lower value in comparison to the critical pressure. In the present solution, the minimum static pressure at the passage to the production well intake is nearly 540 bars. The value is quite above the critical one. Thus, a sCO_2 can be used throughout the entire solution domain.

3.3. Initial and Boundary Conditions

Six surfaces bound the prismatic solution domain, where two vertical surfaces are defined to be symmetry planes as already mentioned above (Figure 4b). The remaining four surfaces are modelled as solid walls with prescribed temperature. The temperatures at the upper and lower horizontal walls that bound the domain are indicated as T_U and T_L, respectively, in Figure 4b. These temperatures are assumed to be constant and prescribed as boundary conditions at these surfaces with the values T_U=138°C and T_L=240°C according to the data provided by Hou et al. (2015), along with the assumption of stagnant fluid. At the beginning of the process, a linear variation of the temperature between the upper and lower walls is assumed, which is applied as initial condition throughout the whole domain, as well as the boundary condition on the vertical wall boundaries.

There is a large-scale difference between domain size and borehole diameters. This makes a coupled modelling of the piping with the rest of the domain very difficult due to extreme grid resolution requirements. Therefore, at present, it is seen that calculating the heat transfer and flow in the pipes in a coupled manner with the outer domain is not appropriate. This may be considered to be a reasonable assumption for current purposes, since the borehole casing is cemented with very low thermal conductivity. As a result, the modeled outer surface of the casing of the wells is considered as adiabatic walls. The inlet boundary of the solution domain is positioned at the outlet of the injection pipe (indicated by a blue dot in Figure 4b). The outlet boundary of the solution domain is positioned at inlet plane of the production pipe (indicted by a red dot in Figure 4b). At the inlet surface, a constant 60°C temperature and 215 kg/s mass flow rate are applied as boundary conditions. At the outlet, a constant static pressure and a zero-gradient condition are applied for the velocities. The problem is analyzed for a configuration, where the inlet and outlet boundaries are 1000 m apart (L=1000, Figure 4b) and 590 m lower than the upper rock layer (H=590 m, Figure 4b).

3.4. Numerical Modelling

In the numerical modelling, a 2nd order accurate, bounded backward differencing scheme (Versteeg and Malalasekera, 2007) is applied for time discretization. In general, the time step size to be employed should be carefully checked not only for reasons of stability but also with regard to temporal accuracy. Even if stability criteria might have been met, smaller time steps may still be needed for accuracy (Bit et al., 2020). Since the presently applied discretization scheme is unconditionally stable, not necessarily the stability, but the accuracy is of concern. In the present calculations, a time step size of 6h is applied. This time step size may appear to be too large compared to other transient phenomena encountered in different applications (Bit et al., 2020). However, in the previous analysis (Benim et al., 2018 *a, b*), it was shown that this time step size is adequate to obtain very accurate temporal resolution for the present problem. This time-step size results in cell Courant and Fourier numbers (Peyret, 1996) that are much smaller than 1.0 and 0.5, respectively. Thus, with this time step size, even an explicit scheme would lead to a stable solution. In the spatial discretization, the formally a 2nd order accurate upwind scheme is used (Glaister, 1993) except for density, for which a 1st order upwinding is used. The PRESTO! interpolation scheme is used for pressure (Peyret, 1996). The velocity-pressure coupling is treated by the PISO scheme (Versteeg and Malalasekera, 2007). The velocity components are under-relaxed in the iterative procedure within a time step. The underrelaxation coefficient is 0.5. None of the further variables are under-relaxed. For the

convergence criteria for each time step, the threshold values of the normalized residuals are set to 10^{-12} for the energy equation. It is set to 10^{-6} for the remaining equations. The solution domain is discretized by essentially equidistant, orthogonal, block-structured grid with hexahedral finite volumes. The utilized computational grid consists of 185,000 nodes. Benim et al. (2018*a*) found out that the grid ensures sufficiently grid independent solutions.

4. Results and Discussion

The calculated temperature (T) distribution in the y-z symmetry plane through the injection well (Figure 4b) following half a year, one year, five years, and fifteen years of production are shown in Figure 5 and Figure 6 for H_2O and sCO_2 as working fluid, respectively.

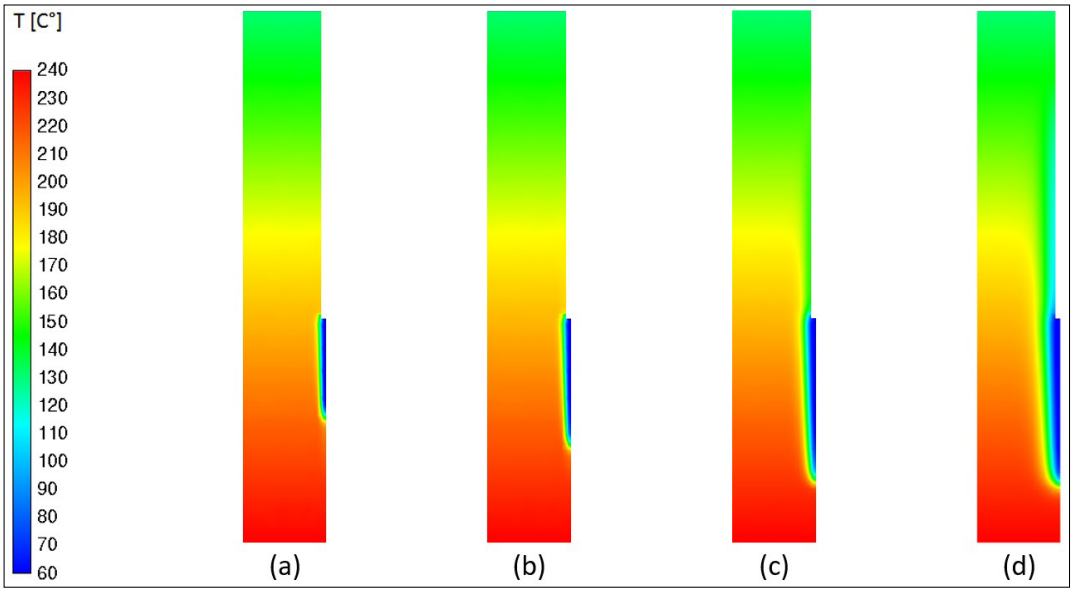

Figure 5- Water as heat transfer fluid: Temperature (°C) variation in y-z symmetry plane (Figure 4b) through the injection well after; a) half a year, b) one year, c) five years, d) fifteen years of production.

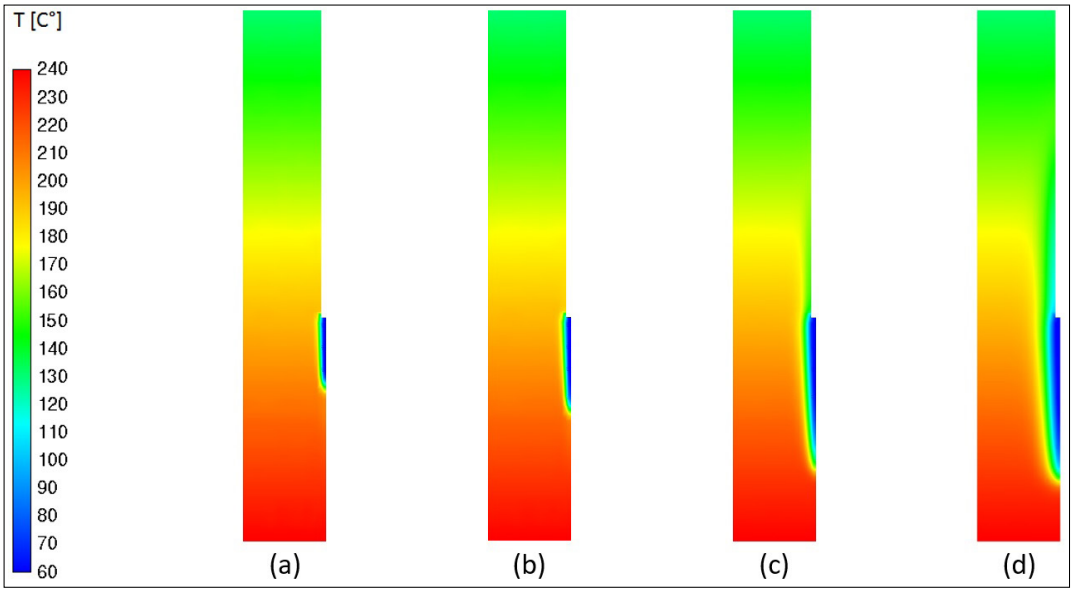

Figure 6- sCO_2 as heat transfer fluid: Temperature (°C) variation in y-z plane (Figure 4b) through the wells; a) half a year, b) one year, c) five years, d) fifteen years of production.

In this plane, with relatively low permeability, the dominant heat transfer mode is conduction (Table 1). The penetration of the temperature front is rather low in y direction. It is rather restricted to the environs of the fractured area. Qualitatively similar behavior is observed for both heat transfer fluids (Figures 5, 6). Quantitatively, the size of the reduced temperature region is smaller for the sCO_2 compared to the water in the early phases of production, and it gradually approaches to that of water in time.

The calculated temperature distribution in the x-z plane (Figure 4b) after half a year, one year, five years, and fifteen years are shown in Figure 7 and Figure 8 for H_2O and sCO_2 as working fluid.

The qualitative features of the temperature patterns are similar for both heat transfer fluids (Figures 7 and 8). After half a year of production, a quite round, nearly elliptic, low temperature region is observed around the injection well (Figures 7a and 8a), which expands further in time while preserving its qualitative shape (Figures 7b, 8b). After five years of production, it can be observed that the shape of the cold zone is distorted with respect to the previous one. In addition, the temperature front has met the lower boundary of the fractured zone and reached the production well (Figures 7c, 8c). After fifteen years of production, one observes that the low temperature zone has further expanded and also reached the lateral boarder of the fractured zone (Figures 7c, 8d). Despite the fact that the cold waterfront reached the production well after about five years, the production temperature still remains above the injection temperature due to the mixing of heated water by its environs of the fractured zone and convective transport of the warmer water into the production well.

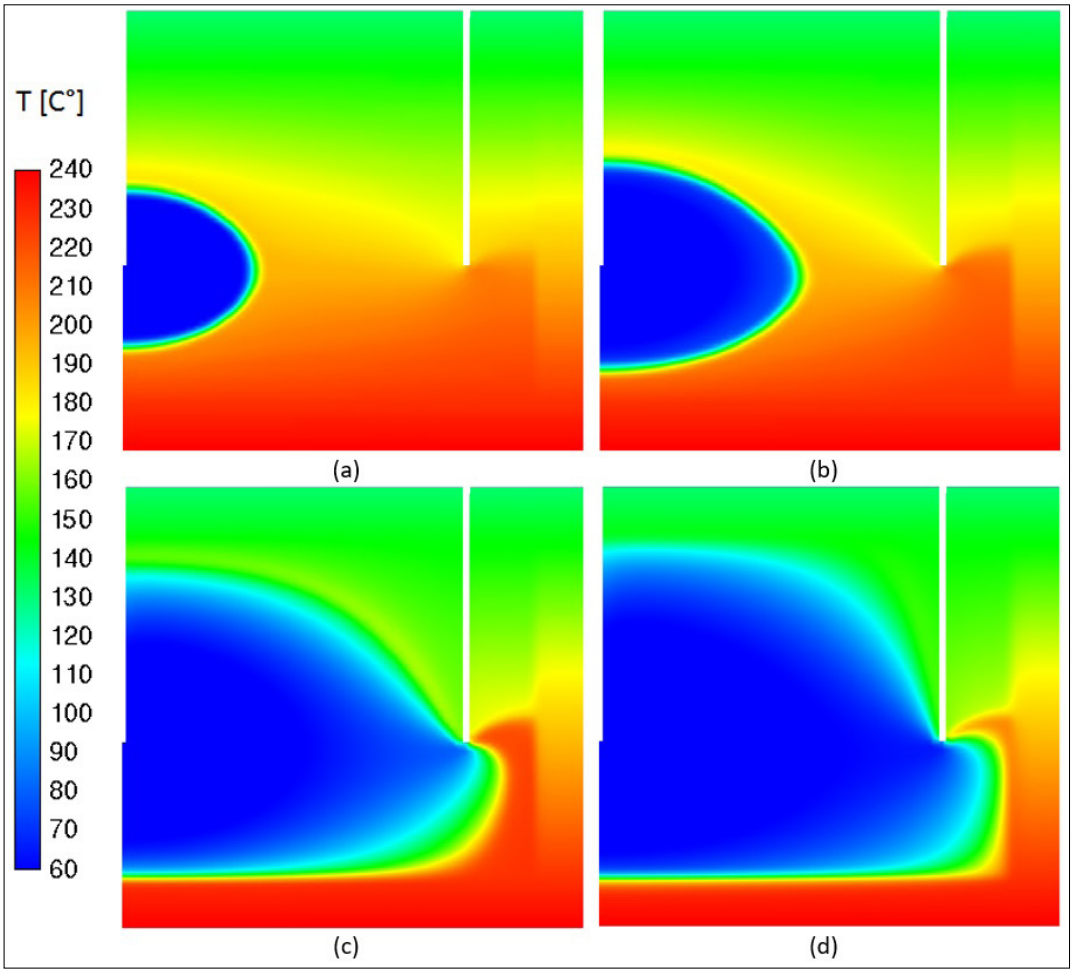

Figure 7- Water as heat transfer fluid: temperature [°C] variation in x-z plane (Figure 4b) through the wells after; a) half a year, b) one year, c) five years, d) fifteen years of production.

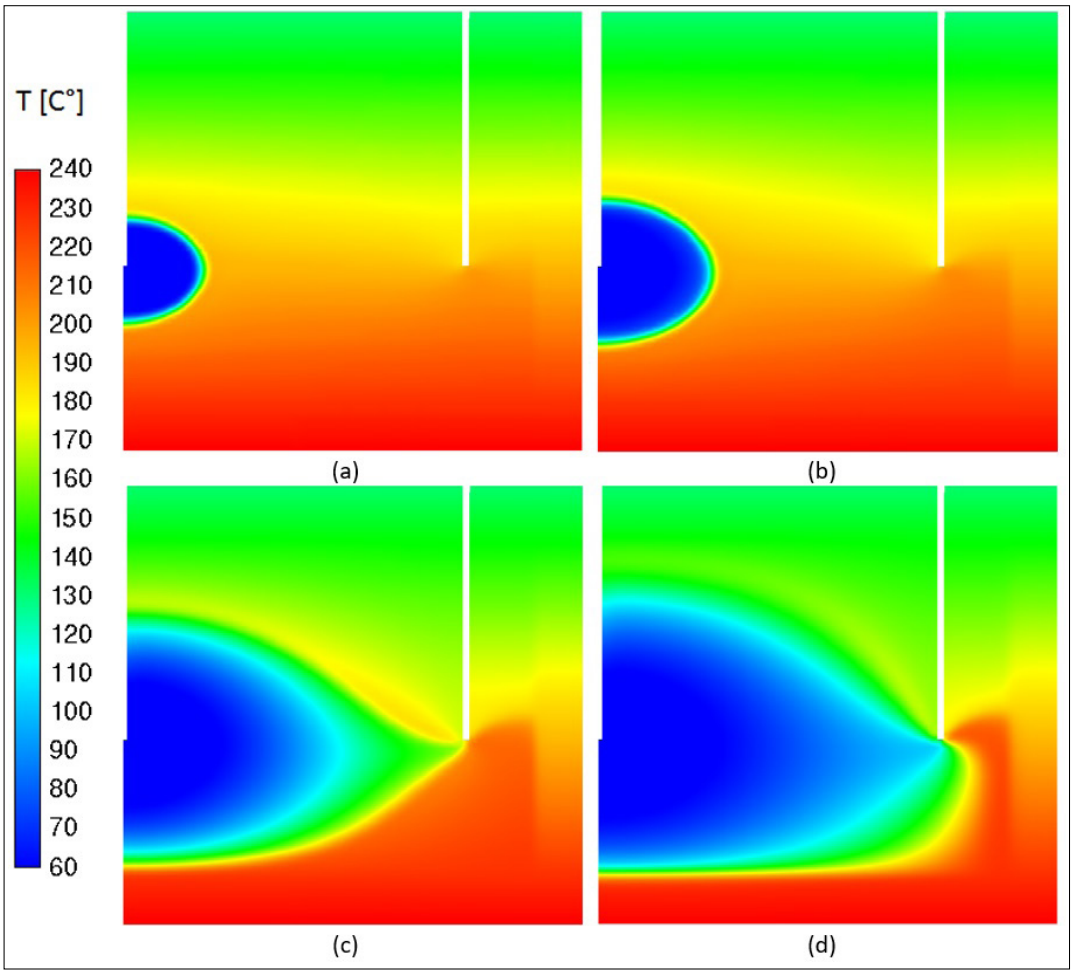

Figure 8- sCO_2 as working fluid: temperature (°C) variation in x-z plane (Figure 4b) through the wells after; a) half a year, b) one year, c) five years, d) fifteen years of production.

One of the significant differences between sCO_2 and water injection is the liquid density variation. The density may vary locally and temporarily depending on temperature-pressure conditions of the working fluid. An obvious result of a variable density is that the CO_2 may be retained in the reservoir, implying that the production flow rate may show a temporal variation and does not need to remain equal to the inlet mass flow during the process. For sCO_2 injection, the calculated flow rate at the production is shown in Figure 9 for 20 years of production. In addition, the constant value for the incompressible water is indicated (any potential loss in working fluid to the ground, a common phenomenon in a real case, is neglected during modeling).

In Figure 9, it is observed that the production flow rate for the sCO_2 is quite low at the beginning, approximately fifty percent of the injection flow rate.

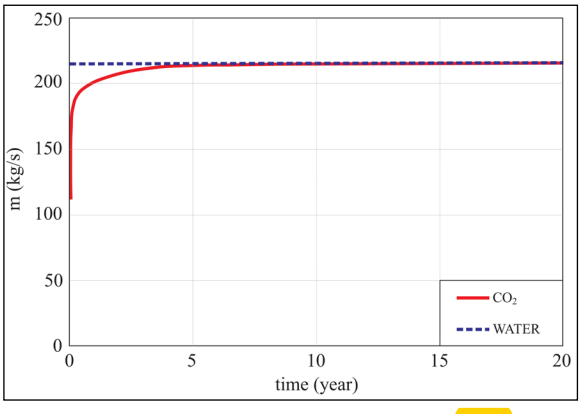

Figure 9- Variation of H_2O and sCO_2 production rates [kg/s] in time.

The value increases quite rapidly in the initial six months and reaches the injection value nearly five years later. Therefore, the storage effect mentioned for sCO_2 is particularly striking within the first five years.

Projected production temperatures for H_2O and sCO_2 during 20 years of production are presented in Figure 10.

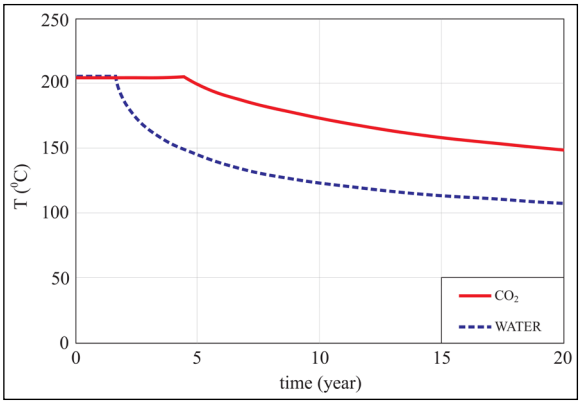

Figure 10- Variation of H_2O and sCO_2 production temperatures (°C) in time.

In the figure, one can see that the temperatures remain constant for an initial period of time and start to decrease thereafter, which is qualitatively the same for both fluids. This time period is shorter for H_2O (nearly one year) compared to subcritical CO_2 (nearly five years). It may be seen in Figure 10 that a much higher production temperature is achieved with sCO_2 over the 20 years of production compared to water. The higher temperatures observed for sCO_2 can be traced back to the differences in the material properties, especially in the thermal conductivity (higher for CO_2) and specific heat capacity (lower for CO_2). At the end of 20 years, the CO_2 production temperature (about 150 °C) is approximately 40 °C higher with respect to water (about 110 °C). In this respect, it is more advantageous to use carbon dioxide instead of H_2O.

The "useful" thermal energy flow rate, i.e. the useful thermal power (P_{TH}) at the production well can be expressed as (Baehr, 2005).

$$P_{TH} = m_P\, c\, (T_P - T_{ref}) \quad (1)$$

where m_P and T_P stand for the production mass flow rate and temperature, respectively, while c denotes the fluid's isobaric specific heat capacity. The reference temperature T_{ref} is taken to be 80°C, with the assumption that this value represents the lowest useful production temperature for which a subsequent energy conversion with acceptable efficiency is possible. The variations of P_{TH} over 20 years for sCO_2 and water injection are presented in Figure 11.

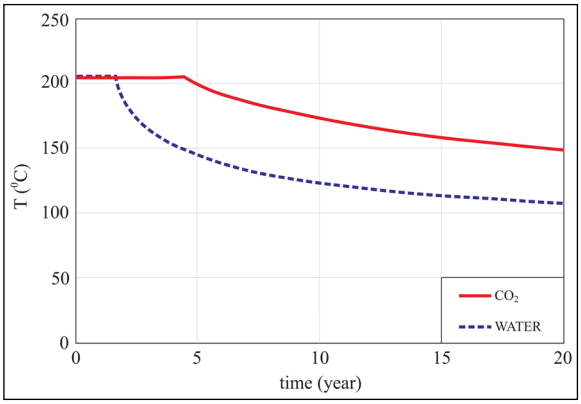

Figure 11- Variation of useful thermal power (MW) in time, for injected H_2O and sCO_2 production.

Although the production temperature of injected water is lower compared to that of sCO_2 (Figure 10), this is compensated and exceeded by the higher specific capacity of water compared to CO_2 so that the production thermal power of water injection turns out to be larger than that of sCO_2 injection, as seen in Figure 11. This is more pronounced in the initial phase of production, where the lower production mass flow rate of sCO_2 (Figure 9) contributes additionally to the lower values of the CO_2 curve. The water curve gradually approaches to the CO_2 curve in time, and reaches practically the same level at the end of the production time of 20 years. At the very beginning of production, the power obtained by water is more than 5 times larger compared to CO_2 for a short time. This ratio rapidly decreases and gets stabilized at about 3 for the first two years of production. Thereafter, the ratio starts to decrease quite rapidly. After five years, the power obtained by water is only about 1.5 times larger compared to CO_2. Beyond fifteen years, the difference is negligible and vanishes towards the end of twenty years period (Figure 11).

The total geothermal energy production using water and sCO_2 as heat transfer fluid over 20 years are depicted in Figure 12, where the curves shown are based on the useful thermal power variations shown in Figure 11. One can see that the total energy produced by CO_2 at the end of 20 years is about 70% of that of water (Figure 12).

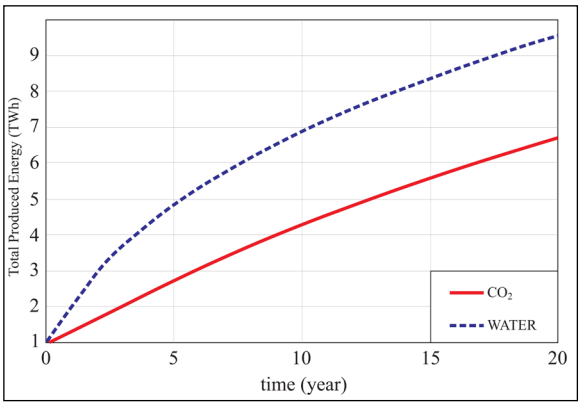

Figure 12- Variation of total produced energy (TWh) in time, for water and sCO_2 as working fluid.

The pressure drops (Δp) in the system and the related loss of mechanical energy is a further important issue, from the energetic point of view. The pressure drops within the solution domain, i.e. between the inlet boundary (at the bottom of the injection well) and the outlet boundary (at the bottom of the production well) can be obtained from the performed numerical calculations. For water injection, the pressure drop in the system remains fairly constant during the whole injection period. In case of sCO_2, a mild increase about 12% is observed within the 20 years of operation time (a mean value is used below).

The mechanical power (P_M), i.e. the pumping power associated with the pressure drop can be estimated from (Streeter and Wylie, 1975).

$$P_M = V\,\Delta p \qquad (2)$$

where V denotes the volume flow rate through the system. In case of sCO_2, the volume flow rate, as well as Δp exhibit local and temporal variations so that spatial and temporal integration processes would be needed to obtain an accurate, representative mean value for P_M. However, since the variations are not too large, an indicative estimation can still be obtained by using approximately averaged values of V and Δp, which is also done currently.

The average pressure drop (Δp) through the system and the associated average mechanical power (P_M) for pumping are presented in Table 3, for water, and sCO_2 as heat transfer fluids.

Table 3- Pressure drop and pumping power for water and sCO_2 injection.

	Δp [Mpa]	**P_M [MW]**
Water	54	12
CO_2	26	8

As one can see in Table 3, the pressure drop for CO_2 is 48% that of water, which may be seen as an advantage for sCO_2 as a working fluid. This difference may obviously be attributed to the difference in the viscosities of both mediums, as the kinematic viscosity of the sCO_2 (on the average) is nearly the half of water. Consequently, the associated mechanical power is smaller for CO_2, compared to water (Table 3). However, ratio of CO_2-to-water is 67% for P_M (Table 3). This is due to the larger volume flow rate (V) of sCO_2. For the same mass flow rate, larger volume flow rates occur for subcritical CO_2, due to its smaller density (on the average) compared to water, causing this trend.

Hou et al. (2015), Benim et al. (2018 *a, b*) studied the EGS potential of the Dikili geothermal field using only water as circulation fluid for 90 days (3 months), 1000 days (nearly 3 years), 10 years and 20 years of production whereas we studied here for 6 months, 1 year, 5 years and 15 years of production for both water and sCO_2. In addition, they used 100, 150, 200 and 250 kg/s steady injection mass flow rates whereas we used only 215 kg/s steady injection mass flow rates during this study. Although the production durations and mass flow rates are different one another, the temperature distributions along x-z and y-z symmetry planes, total produced energy and temperature variations in the outlet of the reservoir seem identical for water. The studies that deal with water and sCO_2 at the same time are scarce even in the world. Based on limited existing studies, some of our findings such as production temperatures, cumulative produced energy and pressure drops for water vs. sCO_2 are comparable with previous studies performed in some other EGS sites such as Zhacanggou, Northeastern Tibet, China (Liu et al., 2019) although geological and modeling parameters are quite different.

5. Conclusions

Higher production temperatures are achieved with sCO_2 as working fluid in comparison to water according to current estimates. It is mainly due to its higher thermal conductivity and lower specific heat capacity, according to current assumptions. However, the thermal energy content of the production may turn out to be lower for sCO_2 as mainly caused by the lower specific heat capacity. On the other hand, as the thermal power varies quite remarkably over the whole production time for water, a more stable production power in time is obtained for sCO_2, which may be seen as an advantage for the latter. A further advantage of the sCO_2 injection is the lower pressure drop due to its lower kinematic viscosity, implying a lower pumping power. The present results encourage a more detailed and comprehensive analysis of the usage of sCO_2, as heat transfer fluid in EGS, including overall system analysis and optimization, which is intended to be considered in the future work. The fact that the use of sCO_2 in EGS may also contribute to the CO_2 storage issue in relationship with the greenhouse effect, the utilization of CO_2 in EGS surely deserves further attention.

References

Altunkaynak, Ş., Yılmaz, Y. 1998. The Mount Kozak magmatic complex, Western Anatolia. Journal of Volcanology and Geothermal Research 85, 211-231.

ANSYS Fluent, 2018. Release 18.0, Theory Guide. https://www.ansys.com/products/fluids/ansys-fluent.

Baba, A., Sözbilir, H., Demir, M. M., Akkurt, G. G., Özşen, A. Y., Şener, M. F., Hancıoğlu, E., Uzelli, T., 2022. İzmir ilindeki jeotermal kaynakların potansiyeli, kullanım alanları, ekonomik ve çevresel etkilerinin belirlenmesi araştırması. Project Report, 194, İzmir.

Baehr, H. D. 2005. Thermodynamik. 12th Edition Springer Verlag, 651.

Benim, A. C. 1990. Finite element analysis of confined turbulent swirling flows. International Journal for Numerical Methods in Fluids 11(6), 697-717.

Benim, A. C., Çiçek, A. 2022. Investigation of the thermohydraulics of an EGS project in Turkey: comparative assessment of water and CO_2 as heat transfer fluid. The International Symposium on Convective Heat and Mass Transfer 5-10 June 2022, İzmir, Turkey.

Benim, A. C., Çiçek, A., Eker, A. M. 2018*a*. A computational investigation of the thermohydraulics of an EGS project. Journal of Thermal Science 27(5), 405-412.

Benim, A. C., Çiçek, A., Eker, A. M. 2018*b*. A Preliminary numerical study of the thermohydraulics of an EGS project in Turkey. MATEC Web of Conferences 240 (1).

Bhattacharyya, S., Chattopadhyay, H., Benim, A. C. 2016. Heat transfer enhancement of laminar flow of ethylene glycol through a square channel fitted with angular cut wavy strip. Procedia Engineering 157, 19-28.

Bit, A., Alblawi, A., Chattopadhyay, H., Quais, Q. A., Benim, A. C., Rahimi-Gorji, M., Do, H. T. 2020. Three-dimensional numerical analysis of hemodynamic of stenosed artery considering realistic outlet boundary conditions. Computer Methods and Programs in Biomedicine 185, 105163.

Bird, R. B., Stewart, W. E., Lightfoot, E. N. 2006. Transport Phenomena. 2nd edition, Wiley, 780.

Borgia, A., Pruess K., Kneafsey, T. J., Oldenburg, C. M., Pan, L. 2012. Numerical simulation of salt precipitation in the fractures of a CO_2 enhanced geothermal system. Geothermics 44(67), 13-22.

Brown, D. 2000. A hot dry rock geothermal energy concept utilizing supercritical CO_2 instead of water, Twenty-Fifth Workshop on Geothermal Reservoir Engineering 24-26 January 2000, Stanford University, 233-238.

Civan, F. 2011. Porous Media Transport Phenomena. Wiley, 488.

Çiçek, A. 2020. The electric power production targeted Unconventional Geothermal Systems (UGS), some conceptual designs and their thermodynamics classification. Bulletin of the Mineral Research and Exploration 163, 211-228.

Emre, Ö., Duman, T. Y., Özalp, S., Elmacı, H., Olgun, Ş., Şaroğlu, F. 2013. 1/250.000 ölçekli Türkiye diri fay haritası. The General Directorate of Mineral Research and Exploration of Türkiye, Special Publications Series, 30, Ankara, Türkiye.

FLAC3D, 2019. Fast Lagrangian Analysis of Continua in Three-Dimensions, Ver. 7.0, Itasca Consulting Group, Minneapolis.

Gürer, F. Ö. 2023. A new look at the origin of N-S trending young basins of western Anatolia. Bulletin of the Mineral Research and Exploration 170, 117-146.

Glaister, P. 1993. Second order accurate upwind difference schemes for scalar conservation laws with source terms. Computers and Mathematics with Applications 25(4), 65-73.

Hou, Z., Şen, O., Gou, Y., Eker, A. M., Li, M., Yal, G. P., Cambazoğlu, S., Were, P. 2015. Preliminary geological, geochemical and numerical study on the first EGS project in Turkey. Environmental Earth Sciences 73, 6747-6767.

Japan International Cooperation Agency (JICA) (1987). Pre-feasibility study on the Dikili Bergama geothermal development project in The Republic of Turkey, Ankara. MTA, Progress Report II, Final Report, 229 .

Lemmon, E. W., Bell, I. H., Huber, M. L., McLinden, M. O. 2018. NIST Standard Reference Database 23: Reference Fluid Thermodynamic and Transport Properties-REFPROP, Version 10.0, National Institute of Standards and Technology, Standard Reference Data Program, Gaithersburg.

Liu, Y., Wang, G., Yue, G., Zhang, W., Zhu, X., Zhang, Q. 2019. Comparison of enhanced geothermal system with water and CO_2 as working fluid: a case study in Zhancanggou, Northeastern Tibet, China. Energy Exploration and Exploitation 37(2), 736-755.

Pan, L., Oldenburg, C. M. 2014. T2 Well -an integrated wellbore-reservoir simulator. Computers and Geosciences 65, 46-55.

Parlaktuna, M., Avşar, U. 2014. Dikili jeotermal sahası kaynak koruma alanları etüt raporu. Middle East Technical University, 163 p., Ankara (unpublished).

Peyret, R,. 1996. Handbook of Computational Fluid Mechanics. Academic Press, 480.

Pruess, K. 1991. TOUGH2: A general-purpose numerical simulator for multiphase fluid flow and heat flow, Lawrence Berkeley Lab., California, USA.

Pruess, K. 2006. Enhanced geothermal systems (EGS) using CO_2 as working fluid – a novel approach for generating renewable energy with simultaneous sequestration of carbon. Geothermics 35, 351-367.

Pruess, K. 2010. Enhanced geothermal systems (EGS) with CO_2 as heat transmission fluid – a scheme for combining recovery of renewable energy with geologic storage of CO_2.World Geothermal Congress 25-29 April 2010, Bali, Indonesia.

Streeter, V. L., Wylie, E. B. 1975. Fluid Mechanics, 6th edition, McGraw-Hill, 752.

Turan, A., Artun, E., Saner, S. 2021. Probabilistic assessment of geothermal resources and their development in Dikili-İzmir region. Earth and Environmental Sciences: Green Energy for Environmental Sustainability, 3, 634.

Uzel, B. 2013. Geological Evolution of İzmir-Balıkesir Transfer Zone: A crustal-scale structure reorganizing extensional tectonics in western Anatolia. Dokuz Eylül University, PhD Thesis, 236.

Versteeg, J. K., Malalasekera, W. 2007. An Introduction Computational Fluid Dynamics – The Finite Volume Method, 2nd edition Pearson, 503.

Whitaker, S. 1986. Flow in porous media I: a theoretical derivation of Darcy's law. Transport in Porous Media 1(1), 3-2.

Wood, B D., He, X., Apte, S. V. 2020. Modeling turbulent flows in porous media, Annular Review of Fluid Mechanics 52, 171-203.

Xia, J. L., Smith, B. L., Benim, A. C., Schmidli, J., Yadigaroğlu, G. 1997. Effect of inlet and outlet boundary conditions on swirling flows. Computers and Fluids 26(8), 881-823.

Yarar, Y. Günaydı, T., Çelebi, N., 2005. Determination of Radon Concentrations of The Dikili Geothermal Area in Western Turkey. Radiation Protection Dosimetry (2006), 118(1), 78-81

Yılmazer, S., Gevrek, A. İ., Sünger, Z., Üstün, Z., Çetiner, L., 1990. İzmir-Dikili-Kaynarca Jeotermal Sahası Kaynarca-1 Derin Jeotermal Sondajı Kuyu Jeolojisi Bitirme ve Değerlendirme Raporu, Maden Tetkik ve Arama Genel Müdürlüğü Report No: 9466, Ankara (unpublished).